The Astrophysical Journal, 973:88 (14pp), 2024 October 1 https://doi.org/10.3847/1538-4357/ad6303

Fundamental Tests of White Dwarf Cooling Physics with Wide Binaries

Manuel Barrientos[1], Mukremin Kilic[1], Pierre Bergeron[2], Simon Blouin[3], Warren R. Brown[4], and Jeff J. Andrews[5]
[1] Homer L. Dodge Department of Physics and Astronomy, University of Oklahoma, 440 W. Brooks Street, Norman, OK 73019, USA; mbarrientos@ou.edu
[2] Département de Physique, Université de Montréal, C.P. 6128, Succ. Centre-Ville, Montréal, QC H3C 3J7, Canada
[3] Department of Physics and Astronomy, University of Victoria, Victoria, BC V8W 2Y2, Canada
[4] Center for Astrophysics, Harvard & Smithsonian, 60 Garden Street, Cambridge, MA 02138, USA
[5] Department of Physics, University of Florida, 2001 Museum Road, Gainesville, FL 32611, USA

Received 2024 April 18; revised 2024 July 1; accepted 2024 July 10; published 2024 September 20

Abstract

We present follow-up spectroscopy and a detailed model atmosphere analysis of 29 wide double white dwarfs, including eight systems with a crystallized C/O core member. We use the state-of-the-art evolutionary models to constrain the physical parameters of each star, including the total age. Assuming that the members of wide binaries are coeval, any age difference between the binary members can be used to test the cooling physics for white dwarf stars, including potential delays due to crystallization and ^{22}Ne distillation. We use our control sample of 14 wide binaries with noncrystallized members to show that this method works well; the control sample shows an age difference of only $\Delta\text{Age} = -0.03 \pm 0.15$ Gyr between its members. For the eight crystallized C/O core systems we find a cooling anomaly of $\Delta\text{Age} = 1.13^{+1.20}_{-1.07}$ Gyr. Even though our results are consistent with a small additional cooling delay (∼1 Gyr) from ^{22}Ne distillation and other neutron-rich impurities, the large uncertainties make this result not statistically significant. Nevertheless, we rule out cooling delays longer than 3.6 Gyr at the 99.7% (3σ) confidence level for 0.6–0.9 $M_\odot$ white dwarfs. Further progress requires larger samples of wide binaries with crystallized massive white dwarf members. We provide a list of subgiant + white dwarf binaries that could be used for this purpose in the future.

Unified Astronomy Thesaurus concepts: Binary stars (154); Wide binary stars (1801); White dwarf stars (1799); Stellar evolution (1599)

Materials only available in the online version of record: figure set

1. Introduction

Stars with initial masses below 8–10 $M_\odot$ expel a significant fraction of their masses to the interstellar medium, leaving behind a white dwarf (WD) as the remnant. These objects typically consist of a C/O core supported by electron degeneracy pressure that constitutes 99% of the mass and surface layers of He and H that account for the remaining 1% (e.g., Saumon et al. 2022). As a WD cools (Mestel 1952), electrostatic interactions become more important than the thermal motion of the ions, leading to the formation of a lattice structure in the center of the star, a process known as core crystallization (Abrikosov 1960; Kirzhnits 1960; Salpeter 1961). This first-order transition from liquid to solid phase releases a considerable amount of latent heat. The extra energy slows down the cooling rate of the WD, resulting in a crystallization sequence in the Hertzsprung–Russell (H-R) diagram (van Horn 1968). Winget et al. (2009) found indirect evidence for crystallization in the WD cooling sequence of the globular cluster NGC 6397, while García-Berro et al. (2010) invoked additional cooling delays from ^{22}Ne sedimentation and C/O phase separation upon crystallization to explain the cooling sequence of the metal-rich open cluster NGC 6791, but direct evidence had to wait another decade.

Thanks to the precise astrometric data from Gaia (Gaia Collaboration et al. 2018), it is now possible to create volume-limited WD samples that provide unbiased estimates of the luminosity and mass functions. Using the Gaia H-R diagram for WDs, Tremblay et al. (2019) found that the crystallization sequence is a mass-dependent pileup in the Gaia H-R diagram, due to the release of latent heat. In addition, they also found strong evidence for additional cooling delays due to element sedimentation and proposed ^{16}O sedimentation as a potential source of these extra delays.

Several authors have studied additional mechanisms for extra energy release related to crystallization and its associated effects. Cheng et al. (2019) investigated the properties of WDs in the so-called *Q*-branch, located in the high-mass end of the WD crystallization sequence, and found that about 6% of the high-mass WDs must experience a ⩾8 Gyr extra cooling delay on the *Q*-branch. They suggested ^{22}Ne settling in the liquid cores of C/O WDs as a source of this extra cooling delay. However, this scenario requires relatively large amounts of ^{22}Ne (6% by mass) to reproduce the observed delay (see Figure 4 in Camisassa et al. 2021).

Instead, Blouin et al. (2021) proposed that the phase separation of ^{22}Ne in a crystallizing C/O WD can lead to a distillation process. Distillation efficiently transports ^{22}Ne toward the center, releasing a considerable amount of gravitational energy. Under a standard WD composition with $X(^{22}\text{Ne}) = 0.014$ and $X(\text{O}) = 0.60$, the phase separation process releases energy after the WD is ∼60% crystallized, creating a cooling delay of ∼1 Gyr for typical $M = 0.6\,M_\odot$ WDs. Blouin et al. (2021) also argued that this mechanism can largely resolve the ultramassive cooling anomaly if the delayed population consists of WDs with moderately above-average ^{22}Ne abundances, $X(^{22}\text{Ne}) = 0.03$. Therefore, ^{22}Ne distillation is a promising solution to the cooling anomaly seen in the Gaia H-R diagram (Bédard et al. 2024).

Although these new physics and observations of the luminosity function are strong tools to test the WD cooling models, the simulations in these works are sensitive to model assumptions such as the star formation rate in our Galaxy (see, e.g., Tremblay et al. 2014; Fantin et al. 2019; Mor et al. 2019; Tremblay et al. 2019; Alzate et al. 2021; Fleury et al. 2022). Another unknown is the core composition, specifically the C/O ratio, which is still poorly constrained (Giammichele et al. 2018). The C/O ratio has a significant impact on the amount of energy released during the phase separation of ^{22}Ne (Blouin et al. 2021).

To avoid population issues, a more direct approach is to study and test the evolutionary models through ages of individual WDs that have gone through crystallization (Venner et al. 2023). The ages of isolated WDs cannot be constrained directly. However, if a WD is located in a star cluster, binary, or multiple-star system, its age can be measured through the other stars in the system. These groups of stars usually contain at least one nondegenerate component from which we can infer the total age of the WDs (e.g., Catalán et al. 2008; Cummings et al. 2018; Barrientos & Chanamé 2021). Venner et al. (2023) identified a Sirius-like quadruple system HD 190412 composed of a crystallizing WD and a nondegenerate triple. The WD (HD 190412 C) is ≈65% crystallized considering a homogeneous C/O core with an O mass fraction of $X(O) = 0.60$, and its age is 4.2 ± 0.2 Gyr, assuming a metallicity of $[Fe/H] = -0.25$. Comparing this value with the system age of $7.3^{+1.9}_{-1.8}$ Gyr, they found an age anomaly of $+3.1 \pm 1.9$ Gyr. The precision of this value is too low to make any statistically significant conclusions about cooling delays from crystallization and its associated effects. However, their findings are consistent with the amplitude of cooling delays expected from ^{22}Ne distillation.

Wide double WD binaries (DWDs) are nature's smallest star clusters. They have traditionally been used to constrain the initial–final mass relation (IFMR) that connects the progenitor main-sequence mass with the final WD remnant mass (Andrews et al. 2015; Hollands et al. 2024). In these systems, the cooling ages, crystallization fractions, and masses of both WDs can be derived using the appropriate spectroscopic and photometric information and the evolutionary models.

In this paper, we aim to constrain the cooling delays in WDs due to crystallization and its associated effects by using DWDs where one of the members is crystallized. Using an IFMR obtained from young and hot WDs in open clusters (e.g., Cummings et al. 2018; Williams et al. 2018), we calculate the progenitor mass and lifetime of both components. Since the open cluster WDs are relatively hot and young, they do not suffer from the cooling delays associated with crystallization, and therefore the resulting IFMR does not suffer from the current problems in our understanding of cooling physics. Hence, the total age of the noncrystallized component can be measured reliably as long as the WD mass is above 0.63 $M_\odot$ (Heintz et al. 2022), providing a benchmark for the whole system. By analyzing the differences in ages between the crystallized and noncrystallized components (ΔAge), we can provide empirical constraints on the cooling delays associated with crystallization and distillation.

We describe our sample selection in Section 2. In Section 3, we present the determination of the atmospheric parameters along with the Bayesian ages for all selected WDs. Section 4 presents our results on the cooling delay and implications for the current evolutionary models. We conclude and summarize the work in Section 5.

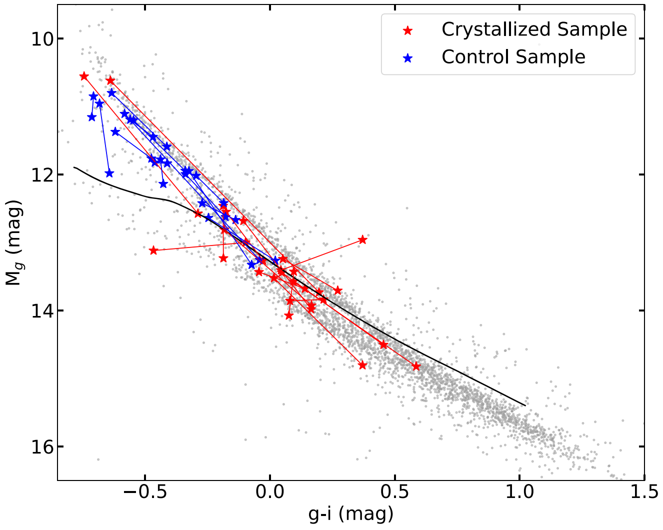

Figure 1. CMD of the selected wide DWDs using Pan-STARRS photometry. The red linked stars show our selected sample where one member is crystallized, the blue linked stars show the control sample where none of the members are crystallized, and the gray circles in the background are WDs within 100 pc of the Sun (Kilic et al. 2020). The black solid line shows the onset of crystallization based on Bédard et al. (2020) models.

2. Wide Binary Sample Selection and Observations

2.1. Sample Selection

El-Badry et al. (2021) identified around 1400 high-probability DWDs, 407 of which have photometry in the Sloan Digital Sky Survey (SDSS) and Panoramic Survey Telescope and Rapid Response System (Pan-STARRS) for both components. Only 82 pairs in this sample have spectral types provided in the literature for both components. In order to identify wide binaries with potentially crystallized components, we use the photometric technique described in Section 3.1 below to constrain the mass and the crystallized core fraction of each WD assuming a pure hydrogen atmosphere (if no spectral information is available) and the C/O core evolutionary models from Bédard et al. (2020). We select binaries with a noncrystallized member and a companion that is ⩾1% crystallized. This reduces our sample to 108 candidate pairs. The crystallization fraction strongly depends on the internal composition and the mass of the WD. Given our assumption of pure H atmospheres for our initial sample selection, the crystallization fractions in this preliminary sample will be reevaluated later in Section 3.2.

Heintz et al. (2022) showed that small uncertainties in WD mass (0.02–0.03 $M_\odot$) correspond to large uncertainties in the progenitor mass and main-sequence lifetimes for WDs with masses below 0.63 $M_\odot$. We further restrict our sample to WDs with $M \geqslant 0.63\,M_\odot$ to avoid this issue. Our preliminary crystallized sample comprises 18 DWDs, 4 of which have spectra available in the literature.

For comparison, we also select a control sample of DWDs where both members are not crystallized and both have masses above 0.63 $M_\odot$. This sample comprises 14 pairs, most of which were previously analyzed in the literature.

Figure 1 shows the locations of our preliminary sample of crystallized systems (red linked stars) along with the control sample (blue linked stars) in a color–magnitude diagram (CMD) using the Pan-STARRS photometry. Gray circles in the background represent the 100 pc WD sample by Kilic et al. (2020), and the black solid line is the onset of crystallization based on the Bédard et al. (2020) models. A few of the WDs in the preliminary crystallized sample appear slightly above the crystallization onset curve. However, classification based on a single CMD can be misleading, as the core crystallization fraction strongly depends on the mass and effective temperature, which require precise constraints on the atmospheric composition. Hence, a detailed model atmosphere analysis of each system is necessary to constrain their physical parameters, as discussed below in Section 3.2.

2.2. Observations

Out of the 18 systems in our preliminary selection, we targeted the 14 systems without optical spectroscopy in the literature for follow-up spectroscopy observations and succeeded in observing 11 of the pairs. We obtained follow-up optical spectroscopy of five pairs using the 8.1 m Gemini North and South telescopes located in Cerro Pachón, Chile, and Maunakea, Hawaii, respectively. We were awarded time to observe three additional pairs at Gemini, but those observations could not be completed in the Gemini queue.

We used the Gemini Multi-Object Spectrograph (GMOS-N and GMOS-S) as part of the queue programs GN-2023A-Q-225, GN-2023A-Q-325, and GS-2023A-Q-325. We used the 1.″0 slit and the B600 grating centered at 515 nm with GMOS-S, providing wavelength coverage from 3670 to 6800 Å and a resolution of 2.0 Å pixel^{-1} in the 4×4 binned mode. We oriented the slit to match the binary position angle so that both components were observed at the same time. We used the same slit, central wavelength, and binning for our Gemini North observations but used the B480 grating, which provides improved sensitivity and wavelength coverage.

We obtained follow-up optical spectroscopy of six pairs using the Blue Channel Spectrograph (Schmidt et al. 1989) on the 6.5 m MMT. We used the 500 line mm^{-1} grating and the 1.″25 slit, which provides a wavelength coverage of 3800–6900 Å and a spectral resolution of 4.7 Å. We reduced the data from both telescopes using the standard IRAF routines. In particular, we used the GMOS package in IRAF for the Gemini-GMOS data. All of our data have signal-to-noise ratio above 15 pixel^{-1}, enabling accurate spectral classification of each system.

2.3. Literature Spectra

For the control sample of 14 pairs where both components are more massive than 0.63 $M_\odot$ and are not crystallized, we found optical spectra for six pairs in Andrews et al. (2015), which were observed at the Apache Point Observatory 3.5 m telescope. We found spectra for six additional pairs in the Montreal White Dwarf Database (MWDD;[6] Dufour et al. 2017). For one of the pairs, the J0859+4250 binary, we could not find an optical spectrum and instead relied on the spectral classification in the literature. For another pair, we found a spectrum for one of the components, J222236.30−082807.9, but not the other member.

3. Analysis

3.1. Model Atmosphere Analysis

To get an accurate estimation of the physical properties of our WD sample, we use the photometric technique described in Bergeron et al. (2019). We apply this approach to our analysis using the SDSS *u* and Pan-STARRS (Chambers et al. 2016) *grizy* photometry. Briefly, this method involves transforming the observed magnitudes in the different bandpasses into average fluxes by using the correct zero-points. Then, using appropriate model atmospheres and chemical compositions, synthetic fluxes are generated and compared to these observed fluxes via χ^2 minimization to derive the best-fitting parameters and their uncertainties. We fit for the effective temperature and the solid angle, $\pi(R/D)^2$, where D is the distance to the star and R is the radius. Since distances are known from Gaia parallaxes (Bailer-Jones et al. 2021), we can constrain the radius of the star directly and, therefore, the gravity (logg parameter) and the mass using Bédard et al. (2020) evolutionary models. Considering the distances of our sample ($d > 100$ pc), we also correct for reddening by using the `STILISM`[7] values (Lallement et al. 2014; Capitanio et al. 2017). The details of our fitting method are further discussed in Kilic et al. (2020).

Figure 2 shows the results from this analysis for one of the pairs. For each star, the top panel shows the SDSS *u* and Pan-STARRS *grizy* photometry (error bars), along with the predicted fluxes from the best-fitting model (filled and open circles). The labels in the same panel give each source's Gaia source ID, object name, and best-fitting parameters. The middle panel shows the predicted spectrum (red line) based on the pure hydrogen solution, along with the observed spectrum in the Hα region, and the bottom panel shows the entire spectrum for each star.

The brighter object in the first pair shown in Figure 2, J002925.62+001552.7 (right panel), is a DA WD that shows Balmer lines, and the best-fitting pure H atmosphere model has $T_{\mathrm{eff}} = 9787 \pm 148$ K. The fainter companion, J002925.29+001559.7 (left panel), is a DC WD with no visible absorption features. If this were a pure H atmosphere, we would have seen a relatively strong Hα line, the absence of which indicates that the atmosphere is dominated by helium. Here the best-fitting helium-rich model has $T_{\mathrm{eff}} = 8601 \pm 156$ K, and the abundance ratio of H to He is given by log H/He = −5.0. The evolutionary models predict that the former has a mass $M = 0.68 \pm 0.04\ M_\odot$ and is not crystallized, whereas the latter has a mass $M = 0.88 \pm 0.04\ M_\odot$ and its core is ∼37% crystallized. This is one of the benchmark systems used in this work to constrain the cooling delay in WDs. The complete figure set of model fits is available in the online version of this article.

Our preliminary crystallized sample comprises eight DA−DA pairs, three DA−DQ pairs, two DAH−DA pairs, one DA−DC pair, and another DAH−DC pair. On the other hand, the control sample comprises 13 DA−DA pairs and one DA−DC pair. For the three DQs in our sample, we rely on the models by Blouin et al. (2019). In this case, we use neutral C I lines or the C_2 Swan band to fit for C/He. We fit both the photometric and spectroscopic data in an iterative process until we converge to a consistent solution. For the magnetic WDs in our sample, we use a similar approach to Moss et al. (2024), where the total line opacity is calculated as the sum of the individual Stark-broadened Zeeman components (see Moss et al. 2024, for further details).

---

[6] https://www.montrealwhitedwarfdatabase.org/

[7] https://stilism.obspm.fr/

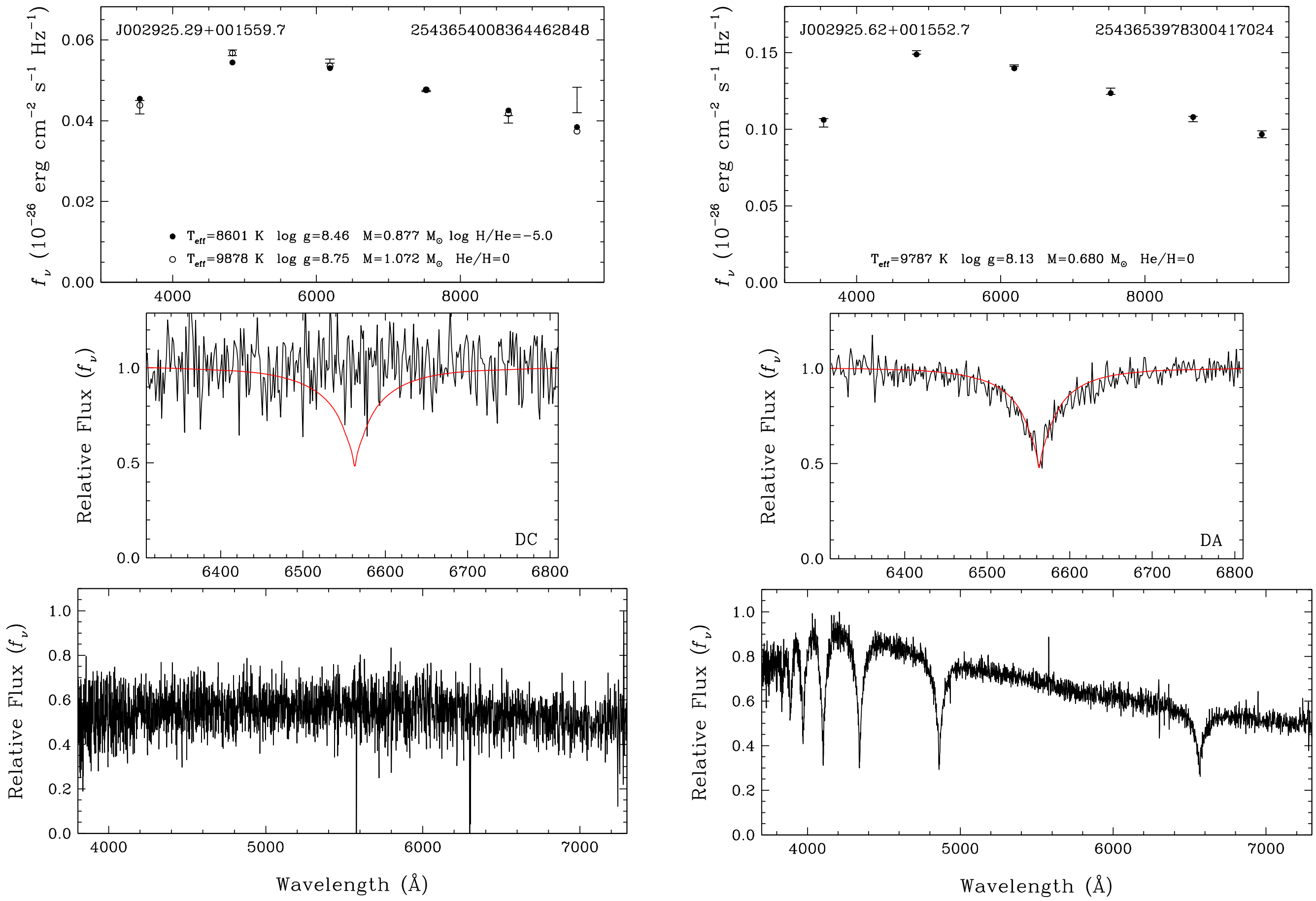

Figure 2. Example model fits for one of the pairs in our sample, including J002925.29+001559.7 (left panel) and J002925.62+001552.7 (right panel). The top panels show the best-fitting pure hydrogen (open circles in the left panel and filled circles in the right panel) and helium-rich (filled circles in the left panel) atmosphere WD models to the SDSS *u* and Pan-STARRS *grizy* photometry (error bars). The best-fitting parameters for each star are included in each panel. The fit for J002925.29+001559.7 favors the He-rich solution, and J002925.62+001552.7 favors a pure H atmosphere solution. The middle panels show the observed spectrum (black) in the Hα region and the predicted Hα (red) based on a pure H solution. The bottom panel shows the full spectral range for each observation, revealing additional H lines for J002925.62+001552.7 and no lines for J002925.29+001559.7. In this case, the WD on the left has a mass of 0.88 $M_\odot$ and a core that is 37% crystallized, whereas the star on the right has a mass of 0.68 $M_\odot$ and 0% crystallization of the core. This is one of the benchmark systems in this work.

(The complete figure set (15 images) is available in the online article.)

Tables 1 and A1 present the best-fitting physical parameters for our preliminary crystallized sample and control sample, respectively, including $T_{\rm eff}$, $\log g$, and mass.

3.2. White Dwarf Age Determination

In order to obtain the total age of a WD, we need to determine both the cooling age ($\tau_{\rm cool}$) and the progenitor lifetime ($\tau_{\rm prog}$). The former is the time since the star ended up on the WD cooling track, and the latter is the time from the zero-age main sequence to the first thermal pulse of the asymptotic giant branch (e.g., Barrientos & Chanamé 2021; Heintz et al. 2022). The best-fitting model parameters and the evolutionary models enable us to constrain the cooling age of each WD. However, determining the progenitor lifetime is more complex, as we have to rely on an empirically calibrated IFMR to trace back the star's initial mass on the main sequence and calculate its lifetime.

To calculate the progenitor mass of each WD, we take advantage of the Bayesian method implemented in `wdwarfdate`[8] by Kiman et al. (2022). We use the best-fitting effective temperature and log*g* from our model atmosphere analysis described in Section 3.1, along with the C/O core evolutionary models by Bauer (2023) and O/Ne core cooling sequences by Camisassa et al. (2019) to calculate the cooling age, $\tau_{\rm cool}$. We also use the `MIST`-based IFMR from Cummings et al. (2018) and MIST evolutionary tracks from Choi et al. (2016) to estimate the initial mass and the $\tau_{\rm prog}$. Since the tangential velocities of our sample are consistent with the thin disk and solar neighborhood kinematics (Chiba & Beers 2000), we use [Fe/H] = 0.0 and no rotation ($v/v_{\rm crit} = 0$). The total age of the WD is obtained by adding $\tau_{\rm cool}$ and $\tau_{\rm prog}$ (see Kiman et al. 2022 for potential caveats). A major source of uncertainty in the WD age determination is the $\tau_{\rm prog}$ calculation. We discuss the sensitivity of our results to the assumed IFMR and the progenitor star metallicity in Section 4.2. The cooling ages, progenitor lifetimes, and total ages for the preliminary crystallized sample and the control sample are presented in Tables 1 and A1, respectively.

One of the WDs in our sample, J211657.92+082048.8, has a mass of 0.49 $M_\odot$, which indicates that it has likely formed through close binary evolution. Hence, this binary was likely a triple system in the past (see, e.g., Andrews et al. 2016; Coutu et al. 2019). Considering that we cannot constrain the age of

---

[8] https://github.com/rkiman/wdwarfdate

Table 1

Selected Wide Double White Dwarfs with a Crystallized Member

Object Name	Gaia Source ID (DR3)	Type	$T_{\rm eff}$ (K)	log(g) (cm s^{-1})	M$_{\rm WD}$ ($M_\odot$)	$\tau_{\rm cooling}$ (Gyr)	$\tau_{\rm progenitor}$ (Gyr)	Total Age (Gyr)	Δ Age[a] (Gyr)	Crystallized Fraction[b] ($M/M_\star$)
J002925.29+001559.7	2543654008364462848	DC	8601 ± 156	8.46 ± 0.04	0.88 ± 0.04	$2.10^{+0.21}_{-0.21}$	$0.24^{+0.06}_{-0.05}$	$2.34^{+0.19}_{-0.18}$	$-0.21^{+1.57}_{-0.57}$	0.37(0.15)
J002925.62+001552.7	2543653978300417024	DA	9787 ± 148	8.13 ± 0.04	0.68 ± 0.04	$0.71^{+0.06}_{-0.05}$	$1.39^{+1.62}_{-0.56}$	$2.11^{+1.57}_{-0.54}$		
J081427.92+013325.6	3089916403229120640	DA	9481 ± 414	8.47 ± 0.14	0.90 ± 0.12	$1.56^{+0.56}_{-0.50}$	$0.25^{+0.20}_{-0.09}$	$1.88^{+0.49}_{-0.33}$	$1.21^{+4.99}_{-1.04}$	0.12(0.00)
J081427.83+013318.7	3089916398933726592	DA	8281 ± 201	8.15 ± 0.14	0.69 ± 0.12	$1.04^{+0.23}_{-0.14}$	$1.96^{+5.04}_{-1.28}$	$3.00^{+5.00}_{-0.95}$		
J102142.06+394225.4	804040486519166976	DA	7692 ± 303	8.29 ± 0.13	0.78 ± 0.12	$1.61^{+0.79}_{-0.37}$	$0.71^{+1.60}_{-0.38}$	$2.69^{+1.05}_{-0.45}$	$0.97^{+5.00}_{-1.29}$	0.18(0.00)
J102141.29+394215.5	804040108562044288	DA	7846 ± 203	8.13 ± 0.12	0.67 ± 0.11	$1.19^{+0.23}_{-0.15}$	$2.15^{+5.08}_{-1.34}$	$3.33^{+5.00}_{-1.05}$		
J105242.54+283252.0	731411283875749760	DA	6171 ± 98	8.24 ± 0.05	0.74 ± 0.04	$3.18^{+0.34}_{-0.32}$	$0.69^{+0.52}_{-0.22}$	$3.97^{+0.35}_{-0.30}$	$4.23^{+4.35}_{-3.57}$	0.41(0.23)
J105242.57+283255.3	731411283874346240	DQ	7061 ± 77	7.95 ± 0.05	0.55 ± 0.05	$1.31^{+0.10}_{-0.09}$	$6.84^{+4.32}_{-3.58}$	$8.18^{+4.34}_{-3.56}$		
J111322.48+323859.0	757911988004305280	DA	7661 ± 75	8.45 ± 0.02	0.88 ± 0.02	$2.77^{+0.14}_{-0.14}$	$0.26^{+0.05}_{-0.05}$	$3.03^{+0.13}_{-0.13}$	$0.82^{+2.99}_{-0.86}$	0.52(0.40)
J111319.38+323818.0	757911884925087104	DA	6882 ± 77	8.09 ± 0.03	0.65 ± 0.03	$1.67^{+0.09}_{-0.08}$	$2.16^{+3.03}_{-0.85}$	$3.85^{+2.99}_{-0.85}$		
J115749.13+313931.0	4026615235380699392	DAH	8734 ± 202	8.44 ± 0.06	0.88 ± 0.05	$1.91^{+0.30}_{-0.30}$	$0.26^{+0.07}_{-0.06}$	$2.17^{+0.27}_{-0.25}$	$2.03^{+4.51}_{-1.29}$	0.28(0.01)
J115749.39+313931.0	4026615235380699520	DA	6996 ± 133	8.08 ± 0.07	0.64 ± 0.06	$1.56^{+0.19}_{-0.15}$	$2.60^{+4.58}_{-1.35}$	$4.18^{+4.51}_{-1.26}$		
J115937.82+134408.7	3920275276810355200	DA	14833 ± 490	9.11 ± 0.02	1.19 ± 0.01	$1.46^{+0.07}_{-0.07}$	$0.06^{+0.01}_{-0.01}$	$1.51^{+0.08}_{-0.07}$	$0.18^{+0.22}_{-0.13}$	0.88(0.77)
J115937.81+134413.9	3920275276810355072	DA	8998 ± 90	8.26 ± 0.02	0.76 ± 0.02	$1.14^{+0.05}_{-0.05}$	$0.53^{+0.23}_{-0.10}$	$1.68^{+0.21}_{-0.10}$		
J123647.95+682501.6	1682366418152856448	DA	6863 ± 116	8.17 ± 0.04	0.70 ± 0.03	$1.95^{+0.22}_{-0.17}$	$1.10^{+0.75}_{-0.43}$	$3.10^{+0.66}_{-0.39}$	$3.57^{+4.70}_{-3.16}$	0.10(0.003)
J123647.42+682502.9	1682554091043762560	DQ	8813 ± 133	7.99 ± 0.03	0.57 ± 0.03	$0.77^{+0.05}_{-0.05}$	$5.79^{+4.71}_{-3.13}$	$6.55^{+4.68}_{-3.11}$		
J134739.13+251228.9	1444442547261998464	DA	6743 ± 104	8.13 ± 0.06	0.67 ± 0.05	$1.88^{+0.24}_{-0.19}$	$1.54^{+2.65}_{-0.67}$	$3.50^{+2.46}_{-0.56}$	$0.02^{+3.23}_{-1.38}$	0.08(0.00)
J134737.58+251233.1	1444442512902260864	DA	8194 ± 133	8.13 ± 0.05	0.67 ± 0.04	$1.10^{+0.10}_{-0.09}$	$1.58^{+2.71}_{-0.69}$	$2.70^{+2.63}_{-0.63}$		
J135834.36+263345.2	1450779342012324224	DA	6717 ± 195	8.29 ± 0.06	0.78 ± 0.05	$2.78^{+0.43}_{-0.43}$	$0.50^{+0.35}_{-0.13}$	$3.38^{+0.36}_{-0.34}$	$-1.31^{+2.64}_{-0.82}$	0.45(0.11)
J135834.66+263343.1	1450779346306149760	DA	21694 ± 453	8.04 ± 0.03	0.65 ± 0.02	$0.06^{+0.01}_{-0.01}$	$1.97^{+2.64}_{-0.73}$	$2.02^{+2.64}_{-0.73}$		
J185722.65+781332.1	2293210651405001216	DA	7709 ± 755	8.25 ± 0.21	0.75 ± 0.19	$1.57^{+1.08}_{-0.48}$	$1.39^{+4.64}_{-0.99}$	$3.48^{+3.98}_{-1.04}$	$-0.38^{+4.10}_{-1.49}$	0.07(0.00)
J185722.00+781332.2	2293210651402924160	DA	8041 ± 120	8.22 ± 0.10	0.73 ± 0.10	$1.26^{+0.37}_{-0.17}$	$1.03^{+2.02}_{-0.57}$	$2.41^{+1.77}_{-0.39}$		
J211658.03+082047.6	1740077893712777216	DA	6302 ± 244	8.15 ± 0.09	0.68 ± 0.08	$2.77^{+0.86}_{-0.61}$	$1.41^{+2.86}_{-0.72}$	$4.40^{+2.88}_{-1.05}$	…	0.22(0.00)
J211657.92+082048.8[c]	1740077893710129536	DQ	7039 ± 90	7.86 ± 0.06	0.49 ± 0.05	$1.33^{+0.12}_{-0.12}$	…	…		
J213102.82+083203.8	1741031891851063424	DA	7065 ± 88	8.26 ± 0.02	0.75 ± 0.03	$2.28^{+0.17}_{-0.17}$	$0.56^{+0.26}_{-0.13}$	$2.88^{+0.23}_{-0.19}$	$0.61^{+3.51}_{-1.26}$	0.25(0.09)
J213103.09+083202.6	1741031896140411648	DA	9048 ± 52	8.06 ± 0.02	0.64 ± 0.02	$0.80^{+0.02}_{-0.02}$	$2.67^{+3.49}_{-1.24}$	$3.47^{+3.51}_{-1.24}$		
J225932.73+140444.2	2815944352131513472	DAH	10768 ± 159	8.49 ± 0.02	0.91 ± 0.02	$1.10^{+0.08}_{-0.06}$	$0.22^{+0.05}_{-0.04}$	$1.32^{+0.08}_{-0.07}$	$-0.96^{+0.09}_{-0.08}$	0.02(0.00)
J225932.21+140439.2	2815944352131513088	DA	27799 ± 402	8.33 ± 0.02	0.84 ± 0.02	$0.03^{+0.00}_{-0.00}$	$0.33^{+0.06}_{-0.05}$	$0.36^{+0.06}_{-0.05}$		
J231939.16-035857.8	2634002940402436480	DAH	5652 ± 52	8.09 ± 0.03	0.64 ± 0.03	$3.13^{+0.24}_{-0.26}$	$2.48^{+3.32}_{-1.11}$	$5.60^{+3.26}_{-1.03}$	$4.65^{+4.52}_{-4.01}$	0.31(0.06)
J231938.65-035833.1	2634003146560869248	DC	6920 ± 80	7.92 ± 0.03	0.53 ± 0.02	$1.29^{+0.07}_{-0.06}$	$8.34^{+3.58}_{-3.70}$	$9.60^{+3.57}_{-3.67}$		

Notes.

[a] ΔAge is the difference in age between the crystallized component and the noncrystallized companion following the Barlow (2003) and Laursen et al. (2019) prescription for asymmetric errors.

[b] Crystallized core fraction for the crystallized component and its 3σ lower limit in parentheses calculated using Bauer (2023) models.

[c] The mass of J211657.92+082048.8 is too small to determine a progenitor mass. Therefore, no age estimation can be made.

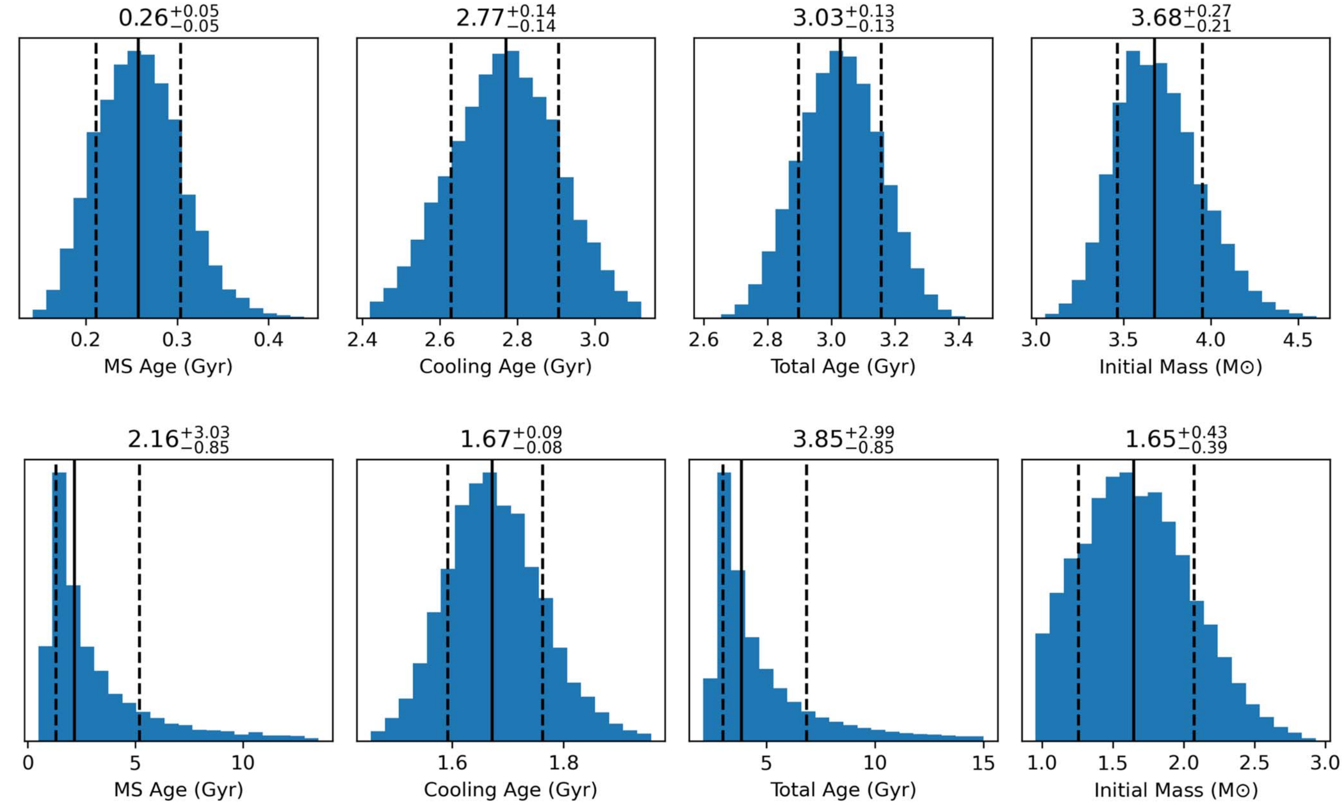

Figure 3. Probability distribution function output of the J1113+3238 pair from `wdwarfdate` by Kiman et al. (2022) for the main-sequence age (or progenitor's lifetime), cooling age, total age of the WD, and initial mass determinations. The calculated values are shown in each panel. In particular, we used Bauer (2023) models to obtain the WD cooling age. The top panels show the parameters for J111322.48+323859.0, a 0.88 $M_\odot$ WD with a ∼5% precision in its total age, whereas the bottom panels show the parameters for a 0.65 $M_\odot$ WD with significantly larger errors in its total age estimate.

this system, we remove it from further consideration, reducing the number of crystallized systems to 14.

An illustration of the `wdwarfdate` output is shown in Figure 3 for the J1113+3238 system. Both panels (top and bottom) show the probability distribution function for the main-sequence age, cooling age, total age, and initial mass of each binary component. The top panel shows J111322.48+323859.0, a 0.88 $M_\odot$ WD with a ∼5% uncertainty in its total age. For comparison, the bottom panel shows J111319.38+323818.0, a 0.65 $M_\odot$ WD with a much more uncertain total age.

We provide a comparison between our results and the parameters obtained by Heintz et al. (2022) in Table A2 and Figure A1 in the Appendix. Heintz et al. (2022) assumed a pure H atmosphere for their targets. The ages from our analysis and Heintz et al. (2022) agree within the errors for the majority of our targets, though we find three significant outliers that are non-DA WDs (DC and DQ spectral types). Since our analysis takes advantage of follow-up spectroscopy of all targets and the model atmospheres with appropriate chemical composition, the physical parameters in this study are more reliable.

Two of the DWDs in our control sample are also included in Hollands et al. (2024). For the J1313+2030 binary, we measure total ages of $0.88^{+0.06}_{-0.05}$ Gyr and $1.19^{+0.43}_{-0.22}$ Gyr for the two components, whereas Hollands et al. (2024) estimated $0.79^{+0.08}_{-0.05}$ Gyr and $0.76^{+0.16}_{-0.08}$ Gyr for the same stars, respectively. Similarly, for the J2223+2201 binary, we estimated $0.44^{+0.04}_{-0.04}$ Gyr and $0.91^{+0.20}_{-0.09}$ Gyr, while they estimated $0.35^{+0.08}_{-0.06}$ Gyr and $0.79^{+0.17}_{-0.12}$ Gyr, respectively. These estimates are consistent with our results within the errors.

We constrain the crystallized core fractions using the C/O core evolutionary models from Bauer (2023) for WDs with $M \leqslant 1.03\ M_\odot$ and the O/Ne core models from Camisassa et al. (2019) for WDs with $M \geqslant 1.10\ M_\odot$. Table 1 includes the crystallized core fraction and its 3σ lower limit in parentheses. We exclude the pairs where the 3σ lower limit indicates a noncrystallized core; specifically, this cut removes the J0814+0133, J1021+3942, J1347+2512, J1857+7813, and J2259+1404 binaries from further consideration, reducing the number of significantly crystallized pairs to nine.

4. Discussion

4.1. Quantifying the Cooling Delays in C/O White Dwarfs

For the nine DWDs with a crystallized member, we estimate the total ages for each WD using the approach explained in detail in Section 3.2. In order to test the age estimates from the current evolutionary models that include the delays from the latent heat and C/O phase separation of crystallization (see Bauer 2023), we calculate the difference in total age, ΔAge, by subtracting the age of the crystallized member from the age of the noncrystallized member. If there are cooling delays that are unaccounted for in the current evolutionary models, then we expect the age of the crystallized member to be underestimated; hence, we expect a positive ΔAge. Since the ages have asymmetric errors and non-Gaussian probability distribution

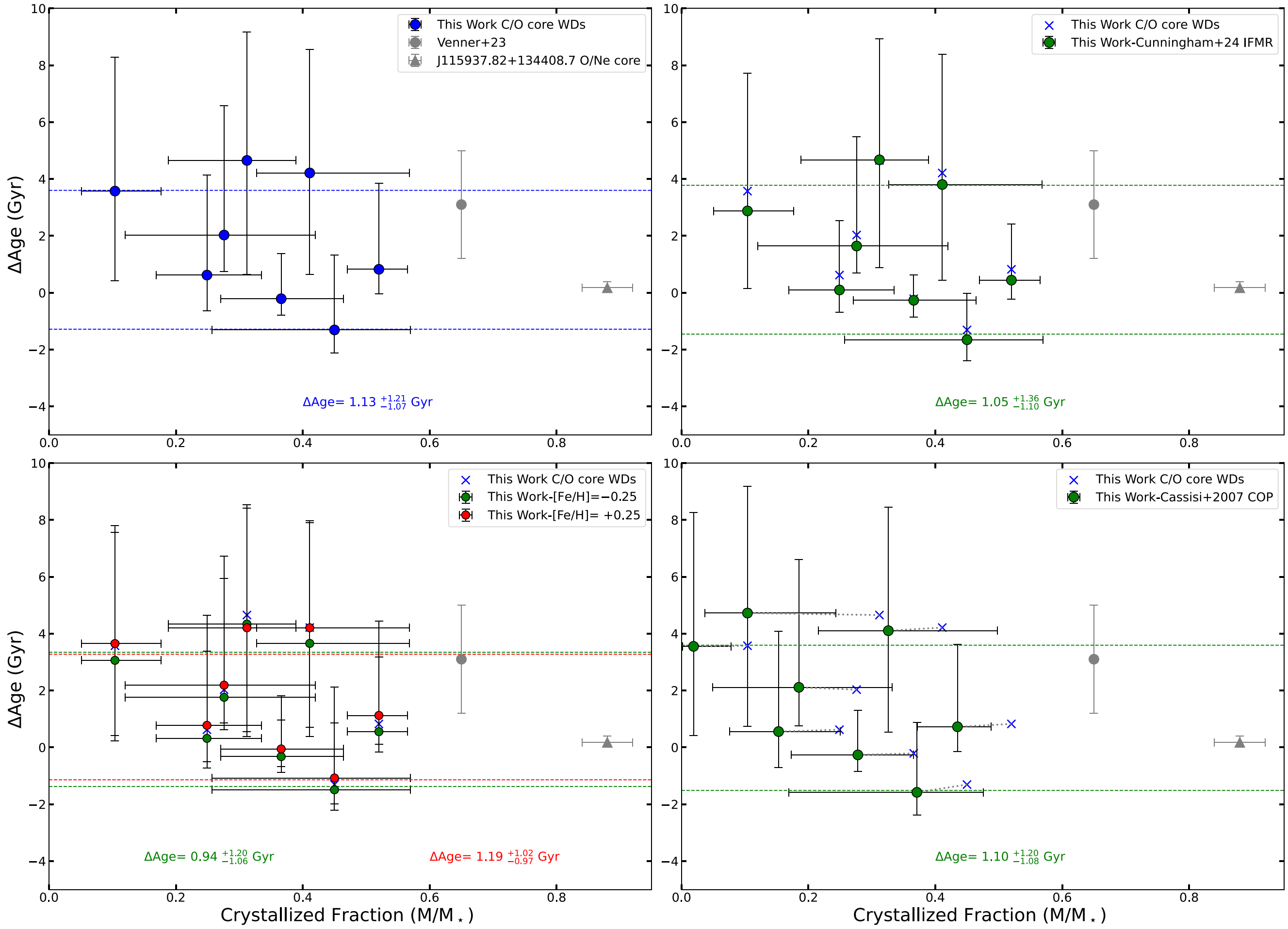

Figure 4. Cooling anomaly in wide DWDs as a function of the crystallized core fraction. The top left panel shows the main results of this work using the prescription described in Section 3.2. The blue circles represent the eight wide DWDs with C/O cores used in this work. The gray circle is the benchmark obtained by Venner et al. (2023), in agreement with our results within 1σ. The gray triangle is an O/Ne WD in our sample that is not part of the analysis. The blue dashed lines show the upper and lower 3σ level (99.7%). We found a weighted mean $\Delta\mathrm{Age} = 1.13^{+1.21}_{-1.07}$ Gyr. The top right panel shows the sensitivity of our results to the IFMR. The blue crosses are our default results (same as the top left panel), the green circles show the ΔAge using the Cunningham et al. (2024) IFMR, and the green dashed line shows upper and lower 3σ levels. In this case, the calculated weighted mean is $\Delta\mathrm{Age} = 1.05^{+1.36}_{-1.10}$ Gyr. The bottom left panel shows the sensitivity of our results to the progenitor star metallicity. Our default results use solar metallicity $[\mathrm{Fe/H}] = 0$ (blue crosses), whereas green and red circles show the ΔAge values for $[\mathrm{Fe/H}] = -0.25$ and $[\mathrm{Fe/H}] = +0.25$, respectively. The green and red lines show the 3σ limits. ΔAge ranges from $0.94^{+1.20}_{-1.06}$ Gyr to $1.19^{+1.02}_{-0.97}$ Gyr for these metallicities. The bottom right panel shows the sensitivity of our results to the conductive opacities used in the cooling models. Our default model (blue crosses) is based on the Bauer (2023) cooling models with electron conductive opacities from Blouin et al. (2020). The green circles show the results when using electron conductive opacities from Cassisi et al. (2007). The green dashed lines show the 3σ limits, and the gray dotted lines show the change from the default results. In this case, $\Delta\mathrm{Age} = 1.10^{+1.20}_{-1.08}$ Gyr.

functions (see Figure 3), we used the approach described in Barlow (2003) and implemented by Laursen et al. (2019, see their Appendix B) to subtract these quantities.[9] For our sample, the crystallized core mass fraction ranges from 10% to 88%, and the masses range from 0.63 to 1.21 $M_\odot$, covering a significant portion of the parameter space for WDs.

We use the J1113+3238 binary to demonstrate our methodology. This binary consists of an $M = 0.86 \pm 0.01\, M_\odot$ WD with a 52% crystallized core and a noncrystallized $M = 0.63 \pm 0.01\, M_\odot$ companion. The cooling age for the crystallized member is $2.77^{+0.14}_{-0.14}$ Gyr. With an estimated progenitor lifetime of $0.26^{+0.05}_{-0.05}$ Gyr, the total age is constrained to $3.03^{+0.13}_{-0.13}$ Gyr. On the other hand, the noncrystallized member has a cooling age of $1.67^{+0.09}_{-0.08}$ Gyr, a progenitor lifetime of $2.16^{+3.03}_{-0.85}$ Gyr, and a total age estimate of $3.85^{+2.99}_{-0.85}$ Gyr. Hence, the evolutionary models underpredict the age of the crystallized member by $\Delta\mathrm{Age} = 0.82^{+2.99}_{-0.86}$ Gyr.

The top left panel of Figure 4 shows the main results of this paper: ΔAge versus the core crystallized mass fraction for our sample of C/O core DWDs (blue circles). The dashed lines show the upper and lower 3σ limits for the sample. Because of the asymmetric errors in the ΔAge measurements, we estimate the weighted mean of the sample by bootstrapping 10,000 times and calculate a weighted mean value using the Barlow (2003) formulation (see their Section 7). After that, we select 50% of the distribution as the mean, 16%–84% as the 1σ uncertainties, and 0.3%–99.7% as the 3σ limits. We find a cooling anomaly of $\Delta\mathrm{Age} = 1.13^{+1.21}_{-1.07}$ Gyr from the eight pairs with a crystallized C/O core member. For comparison, we also plot the Sirius-like benchmark system from Venner et al. (2023), where the cooling anomaly is $+3.1 \pm 1.9$ Gyr (gray circle), and J1159+1344, the only massive WD with a likely O/Ne core in our sample (gray triangle). The latter was not included in our ΔAge estimate (see Section 4.5).

---

[9] We used the Python package `add_asym` (https://github.com/anisotropela/add_asym).

We perform a similar analysis on the 14 binaries in the control sample and find a weighted mean of $\Delta\mathrm{Age} = -0.03 \pm 0.15$ Gyr (see Table A1 for details). This indicates that our method is reliable and that the evolutionary models give consistent results for noncrystallized WDs. Note that these models include the latent heat and the C/O phase separation upon crystallization (Bauer 2023), but not the extra energy from ^{22}Ne distillation. Our sample of DWDs with crystallized members do not show a significant cooling delay, as the ΔAge value is consistent with the null result within the errors. More importantly, we exclude cooling delays from ^{22}Ne distillation and other neutron-rich impurities exceeding 3.6 Gyr for 0.6–0.9 $M_\odot$ WDs at the 99.7% (3σ) confidence level. Even though one may expect a correlation between ΔAge and the crystallized core fraction, we do not observe a significant trend in our sample. Blouin et al. (2021) suggested that the cooling delay from ^{22}Ne distillation may kick in only after the core is 60% crystallized. Unfortunately, all of the C/O core WDs in our DWD sample have core crystallization fractions below this limit.

4.2. Sensitivity to the Initial–Final Mass Relation, Metallicity, and the Conductive Opacities

The ultimate challenge in measuring WD ages is the determination of the progenitor lifetime. To obtain this number, the use of an IFMR to trace back the initial mass and the use of evolutionary tracks to estimate the main-sequence age are essential. The latter also heavily depends on the metallicity.

To test the sensitivity of the total ages to the IFMR, we perform new calculations using the IFMR from Cunningham et al. (2024) for a fixed metallicity $[\mathrm{Fe/H}] = 0$. The top right panel of Figure 4 shows the results using this prescription. The green circles display the ΔAge values for our crystallized sample, blue crosses show the results from the default prescription described in Section 3.2, and the green dashed line shows the upper and lower 3σ limits. The average age discrepancy between both sets is ∼0.36 Gyr. This translates into ΔAge values shifting slightly toward smaller values with a weighted average of $\Delta\mathrm{Age} = 1.05^{+1.36}_{-1.10}$ Gyr. Therefore, the IFMR choice minimally impacts our results.

To test the impact of the progenitor star metallicity on our results, we used two more sets of MIST stellar evolution tracks with $[\mathrm{Fe/H}] = -0.25$ and $+0.25$ (see Rebassa-Mansergas et al. 2021) and no rotation ($v/v_{\mathrm{crit}} = 0$) for a fixed IFMR (Cummings et al. 2018). The bottom left panel of Figure 4 shows the results for this setup. The green and red circles represent the results for $[\mathrm{Fe/H}] = -0.25$ and $[\mathrm{Fe/H}] = +0.25$, respectively; the 3σ limits are shown as the green and red dashed lines, and the blue crosses show our default results. We measure a cooling anomaly ranging from $0.94^{+1.20}_{-1.06}$ Gyr to $1.19^{+1.02}_{-0.97}$ Gyr for this metallicity range, $[\mathrm{Fe/H}] = -0.25$ to $+0.25$. Hence, the choice of the progenitor star metallicity does not significantly impact our results.

Lastly, to test the effects of the electron conductive opacities on the age estimates, we compare our default results that use MESA models from Bauer (2023) and conductive opacities from Blouin et al. (2020) with a MESA model with the same properties but using the conductive opacities from Cassisi et al. (2007). This comparison is displayed as the green circles in the bottom right panel of Figure 4. The green dashed lines mark the 3σ limits. We do not observe any significant differences in age estimates, as all our WDs have cooling ages less than 4 Gyr (see Figure A1 in Bauer 2023). However, the crystallized core fractions change under the assumption of different conductive opacities, decreasing by about 10% for the Cassisi et al. (2007) opacities. This is represented as the dotted lines connecting blue crosses and green circles. Nevertheless, the cooling anomaly, $\Delta\mathrm{Age} = 1.10^{+1.20}_{-1.08}$ Gyr, is similar to the one in our default model.

4.3. ^{22}Ne Distillation

Blouin et al. (2021) demonstrated that the exact shape of the C/O/Ne phase diagram is critical, as it determines the qualitative outcome of the distillation process and whether a ^{22}Ne-rich core or shell is formed. The latter results in a significantly smaller amount of gravitational energy release and a smaller cooling delay. This cooling delay is expected to take place after ∼60% of the core is crystallized, assuming an initially homogeneous C/O profile with $\mathrm{X(O)} = 0.60$. For typical ^{22}Ne mass fractions of 1.4%, the predicted cooling delays are 1.6–2 Gyr for $M = 0.6$–$1.0\,M_\odot$ WDs.

Stellar mergers may produce C/O WDs with significantly larger amounts of heavy neutron-rich impurities like ^{22}Ne. Bédard et al. (2024) present the expected cooling delays from ^{22}Ne distillation in ultramassive WDs that are enriched in ^{22}Ne. They estimate that these stars will form a ^{22}Ne-rich central core, and the resulting distillation process can lead to cooling delays of order 7–13 Gyr depending on the stellar mass (see their Figure 4(a)). They conclude that the cooling delay provided by ^{22}Ne distillation can indeed explain the ultramassive WD cooling anomaly discovered by Cheng et al. (2019). The range of masses analyzed in that work does not overlap with our sample.

There is only a single pair in our sample with a WD that is close to the ∼60% crystallized core fraction. J1113+3238 is the most interesting, as one of its members has a C/O crystallized core fraction of 52%. The parameters for each binary member of this system were discussed in Section 4.1. Most importantly, we measure a relatively small cooling anomaly of $\Delta\mathrm{Age} = 0.82^{+2.99}_{-0.86}$ Gyr for the crystallized WD in this system. Since the models used in our study include the extra energy from the latent heat of crystallization and C/O phase separation, we can isolate the effects of ^{22}Ne distillation. Although the large age uncertainties in our study do not allow us to strongly constrain this effect, we can provide a firm empirical upper limit of 3.6 Gyr (3σ limit) on the cooling delays associated with the distillation of ^{22}Ne or other neutron-rich impurities for WDs with masses between 0.6 and 0.9 $\mathrm{M}_\odot$.

4.4. Convective Coupling

Another important process that affects the cooling rate in WDs is the onset of convective coupling. For massive WDs, convective coupling happens long after the start of crystallization. Hence, its impact on the evolutionary timescales is distinct from crystallization. On the other hand, for regular WDs around 0.6 $M_\odot$, both of these processes overlap, and therefore convective coupling can mask the cooling delays from crystallization alone (e.g., Fontaine et al. 2001). Figure 5 displays the effective temperatures and masses for our sample of DWDs with a crystallized member (black stars), along with the 100 pc WD sample from Kilic et al. (2020; gray circles). The solid black line represents the onset of crystallization for C/O core ($M \leqslant 1.03\,M_\odot$; Bauer 2023) and O/Ne core ($M \geqslant 1.10\,M_\odot$; Camisassa et al. 2019) WDs, whereas the blue

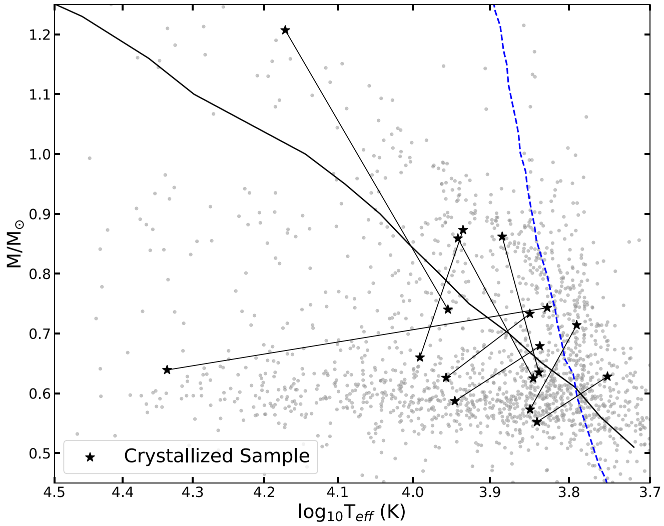

Figure 5. WD masses as a function of the effective temperature for our sample of wide DWDs with a crystallized member (black stars). The gray circles in the background are the 100 pc WD sample from Kilic et al. (2020), the black solid line represents the onset of crystallization based on Bauer (2023) C/O models ($M \leqslant 1.03$) and Camisassa et al. (2019) O/Ne models ($M \geqslant 1.10$), and the blue dashed line shows the onset of convective coupling based on Bédard et al. (2020) models.

dashed line shows the onset of convective coupling (Bédard et al. 2020). Based on this figure, two of the WDs in our analysis have gone through the convective coupling process, J105242.54+283252 and J231939.16-035857. If we further exclude these two pairs from our sample of crystallized WDs, the resulting ΔAge value is slightly lower (∼0.3 Gyr). However, given the relatively large errors in our ΔAge measurement, this change is insignificant.

4.5. No Additional Cooling Delays in a Crystallized O/Ne Core White Dwarf

There is only one DWD in our sample with a member that is more than 60% crystallized: J115937.82+134408.7. This is a DA WD with $T_{\rm eff} = 14833 \pm 490$ K and $M = 1.21 \pm 0.01\, M_\odot$, and it has a core that is 88% crystallized. Assuming that the two stars did not interact during their evolution, J115937.82+134408.7 likely has an O/Ne core, given its high mass. This is consistent with the fact that both stars in this binary appear to be normal DA WDs with disk kinematics. Therefore, we use O/Ne core models from Camisassa et al. (2019) for the massive WD in this binary.

This type of WD crystallizes following a standard scenario where the solid crystals are heavier than the liquid, and therefore they sink to the underlying solid core (Camisassa et al. 2019; Blouin & Daligault 2021). The amount of energy released in this case, from both latent heat and gravitational energy, is significantly smaller than the ^{22}Ne distillation process (see Figure 2(b) in Bédard et al. 2024). Hence, we do not expect to find significant cooling anomalies in O/Ne core WDs.

The companion in this case, J115937.81+134413.9, is a regular C/O core WD with mass $0.74\, M_\odot$ that is not crystallized. We find a cooling anomaly of $0.18^{+0.22}_{-0.13}$ Gyr for this system. Hence, there is no evidence of any extra cooling delays in this likely O/Ne core WD with a core that is significantly crystallized. Since ^{22}Ne distillation cannot take place in O/Ne cores (Camisassa et al. 2019; Bédard et al. 2024), this result is not surprising, but it is reaffirming that the observations find no significant additional cooling delays in this system. This should be compared to the ∼10 Gyr cooling delays inferred for similarly massive WDs, including massive DQs and DAs, on the *Q*-branch (Cheng et al. 2019; Bédard et al. 2024; Kilic et al. 2024).

4.6. The Way Forward: Subgiant + Crystallized White Dwarf Binaries

The ultimate limitation in testing the cooling physics using DWDs is the precision of the age measurements for WDs. We showed here that, even after restricting our sample to WDs with masses above $0.63\, M_\odot$ (Heintz et al. 2022), we still deal with large age uncertainties since it is inherently difficult to obtain precise total ages for typical WDs with $M \sim 0.6\, M_\odot$. The ideal systems for characterizing the cooling delays introduced by ^{22}Ne distillation would involve WDs with well-determined ages and cores that are more than ∼60% crystallized.

Barrientos & Chanamé (2021) presented an alternate sample where the ages of WDs can be determined using their subgiant companions. They used subgiant + WD binaries to constrain the IFMR by relying on the precise age dating of the subgiant companions. A similar approach can be considered using main-sequence + WD binaries as done in Rebassa-Mansergas et al. (2023).

We selected a sample of ∼60 binaries from El-Badry et al. (2021) where the primary star is a subgiant and the secondary is a crystallized WD based on the Bédard et al. (2020) models. Table A2 presents a list of these newly identified pairs with Gentile Fusillo et al. (2021) parameters for the WDs. This alternate sample has the potential to provide better system ages for these pairs containing crystallized WDs. We encourage and plan on obtaining follow-up observations of the most interesting systems in this sample to characterize their system parameters and empirically constrain the cooling delays from ^{22}Ne distillation and other associated effects.

5. Summary and Conclusions

We present a detailed model atmosphere analysis of 29 wide DWDs, including nine systems where one of the members is crystallized. We selected these high-confidence binaries from El-Badry et al. (2021) and obtained spectroscopic follow-up for the targets with no spectral information in the literature. Our final sample includes WDs with crystallized core fractions of 10%–88%.

We used a Bayesian approach to calculate the cooling age, progenitor lifetime, and total age of each star, and then we used these ages to search for cooling anomalies in the crystallized members. We take the total age of the noncrystallized star as the true age of each binary. We find a cooling anomaly of $\Delta{\rm Age} = 1.13^{+1.20}_{-1.07}$ Gyr for the eight binaries with crystallized WDs and C/O cores. The same analysis on the control sample gives $\Delta{\rm Age} = -0.03 \pm 0.15$ Gyr, indicating that this method gives reliable results.

Our results are consistent with the null hypothesis; given the relatively large errors, we do not find a significant cooling anomaly in our sample of eight DWDs with crystallized C/O core members. More importantly, we can rule out cooling anomalies larger than 3.6 Gyr due to ^{22}Ne distillation and other neutron-rich impurities at the 99.7% (3σ) confidence level for WDs of masses between 0.6 and 0.9 $M_\odot$.

The use of wide binaries with at least one WD component provides a new way to test the cooling physics of these objects. In particular, we present a sample of ∼60 binaries composed of a subgiant star with a crystallized WD companion. The subgiant can be age-dated precisely to estimate the total system age, which can then be used to infer any cooling anomalies present in the crystallized WD companion. Future analysis of these pairs can help us obtain and improve age measurements and therefore bring us closer to empirically constraining the cooling delays in WDs.

Acknowledgments

We thank the referee for useful comments that greatly improved this manuscript. M. K. acknowledges the support by the NSF under grant AST-2205736; by NASA under grants 80NSSC22K0479, 80NSSC24K0380, and 80NSSC24K0436; by the NSERC Canada, the Fund FRQ-NT (Québec), and the Canadian Institute for Theoretical Astrophysics (CITA) National Fellowship Program; and by the Smithsonian Institution.

Based on observations obtained at the MMT Observatory, a joint facility of the Smithsonian Institution and the University of Arizona.

Based on observations obtained at the international Gemini Observatory, a program of NSF's NOIRLab, which is managed by the Association of Universities for Research in Astronomy (AURA) under a cooperative agreement with the National Science Foundation on behalf of the Gemini Observatory partnership: the National Science Foundation (United States), National Research Council (Canada), Agencia Nacional de Investigación y Desarrollo (Chile), Ministerio de Ciencia, Tecnología e Innovación (Argentina), Ministério da Ciência, Tecnologia, Inovações e Comunicações (Brazil), and Korea Astronomy and Space Science Institute (Republic of Korea).

Appendix
Data Tables and Figures

In this appendix, we show additional tables and a figure as part of this work. In Table A1, we provide the physical parameters of the control sample used in this work. Table A2 and Figure A1 present an age comparison of the binary systems analyzed here and in Heintz et al. (2022). In Table A3, we provide a list of candidate subgiant + crystallized WD binaries for future studies.

Table A1
The Physical Parameters for the Double White Dwarfs in Our Control Sample

Object Name	Gaia Source ID (DR3)	Type	$T_{\rm eff}$ (K)	$\log(g)$ (cm s^{-1})	$M_{\rm WD}$ ($M_\odot$)	$\tau_{\rm cooling}$ (Gyr)	$\tau_{\rm progenitor}$ (Gyr)	Total Age (Gyr)	Δ Age[a] (Gyr)
J003051.80+181046.0	2794800060629297152	DA	14366 ± 292	8.28 ± 0.05	0.75 ± 0.03	$0.34^{+0.04}_{-0.04}$	$0.47^{+0.26}_{-0.11}$	$0.82^{+0.24}_{-0.09}$	$0.40^{+0.58}_{-0.32}$
J003051.75+181053.7	2794800056333855232	DA	13633 ± 234	8.20 ± 0.05	0.70 ± 0.03	$0.33^{+0.04}_{-0.03}$	$0.82^{+0.57}_{-0.30}$	$1.15^{+0.56}_{-0.27}$	
J080333.78-090705.8	3039398650000089472	DA	11247 ± 130	8.07 ± 0.02	0.63 ± 0.01	$0.46^{+0.02}_{-0.02}$	$2.25^{+3.14}_{-0.89}$	$2.73^{+3.10}_{-0.91}$	$0.92^{+3.51}_{-1.57}$
J080333.92-090658.4	3039398650000089600	DC	7933 ± 177	8.11 ± 0.03	0.65 ± 0.02	$1.19^{+0.10}_{-0.09}$	$1.68^{+2.35}_{-0.63}$	$2.87^{+2.28}_{-0.61}$	
J082730.72-021618.5	3072961074934467200	DA	27037 ± 980	8.60 ± 0.04	0.97 ± 0.02	$0.10^{+0.02}_{-0.02}$	$0.14^{+0.03}_{-0.02}$	$0.24^{+0.03}_{-0.03}$	$0.17^{+0.08}_{-0.07}$
J082730.58-021620.1	3072961070640767488	DA	24501 ± 930	8.33 ± 0.04	0.81 ± 0.03	$0.07^{+0.02}_{-0.01}$	$0.34^{+0.08}_{-0.06}$	$0.41^{+0.07}_{-0.06}$	
J085917.36+425031.6	1008929564913828224	DA	9707 ± 153	8.14 ± 0.04	0.66 ± 0.03	$0.73^{+0.06}_{-0.06}$	$1.36^{+1.47}_{-0.58}$	$2.10^{+1.44}_{-0.54}$	$0.88^{+3.26}_{-1.27}$
J085917.23+425027.4	1008929569208837376	DA	11106 ± 117	8.09 ± 0.04	0.64 ± 0.02	$0.48^{+0.03}_{-0.03}$	$2.00^{+3.14}_{-0.83}$	$2.49^{+3.15}_{-0.81}$	
J092513.18+160145.4	630770819920096768	DA	21766 ± 442	8.83 ± 0.01	1.10 ± 0.01	$0.49^{+0.03}_{-0.03}$	$0.08^{+0.01}_{-0.01}$	$0.57^{+0.03}_{-0.03}$	$-0.20^{+0.05}_{-0.05}$
J092513.48+160144.1	630770819920096640	DA	24050 ± 482	8.40 ± 0.02	0.85 ± 0.01	$0.09^{+0.01}_{-0.01}$	$0.27^{+0.05}_{-0.04}$	$0.36^{+0.05}_{-0.04}$	
J100244.88+360629.6	795886439568266368	DA	10428 ± 176	8.23 ± 0.06	0.71 ± 0.03	$0.70^{+0.09}_{-0.07}$	$0.72^{+0.61}_{-0.25}$	$1.43^{+0.55}_{-0.20}$	$1.78^{+4.09}_{-1.14}$
J100245.86+360653.3	795886439568268032	DA	9471 ± 135	8.09 ± 0.06	0.63 ± 0.03	$0.72^{+0.07}_{-0.06}$	$2.33^{+4.11}_{-1.12}$	$3.04^{+4.09}_{-1.07}$	
J111020.98+451801.7	782193985044906752	DA	20511 ± 348	8.11 ± 0.02	0.67 ± 0.01	$0.08^{+0.01}_{-0.01}$	$1.25^{+0.69}_{-0.47}$	$1.33^{+0.69}_{-0.47}$	$1.21^{+2.66}_{-0.95}$
J111016.68+451736.3	782194019404645632	DA	12992 ± 180	8.07 ± 0.01	0.64 ± 0.01	$0.32^{+0.01}_{-0.01}$	$2.07^{+2.62}_{-0.75}$	$2.38^{+2.65}_{-0.74}$	
J122717.81+563821.7	1574653689250595072	DA	8543 ± 225	8.13 ± 0.05	0.65 ± 0.03	$0.99^{+0.11}_{-0.09}$	$1.54^{+2.46}_{-0.66}$	$2.55^{+2.36}_{-0.60}$	$-0.04^{+2.91}_{-1.31}$
J122717.42+563825.6	1574653689250360576	DA	17013 ± 422	8.08 ± 0.03	0.65 ± 0.02	$0.15^{+0.01}_{-0.01}$	$1.66^{+2.21}_{-0.61}$	$1.81^{+2.20}_{-0.61}$	
J131332.14+203039.6	3940068410255312768	DA	12670 ± 154	8.35 ± 0.01	0.81 ± 0.01	$0.56^{+0.03}_{-0.02}$	$0.35^{+0.06}_{-0.05}$	$0.91^{+0.06}_{-0.05}$	$0.41^{+0.46}_{-0.31}$
J131332.56+203039.4	3940068414551140608	DA	12789 ± 137	8.16 ± 0.01	0.69 ± 0.01	$0.38^{+0.01}_{-0.01}$	$0.94^{+0.45}_{-0.31}$	$1.32^{+0.46}_{-0.30}$	
J170355.91+330438.4	1337576648471644800	DA	9932 ± 126	8.24 ± 0.03	0.73 ± 0.01	$0.85^{+0.05}_{-0.05}$	$0.59^{+0.29}_{-0.14}$	$1.45^{+0.27}_{-0.13}$	$0.71^{+1.79}_{-0.57}$
J170356.77+330435.7	1337576648471644288	DA	11120 ± 131	8.10 ± 0.02	0.65 ± 0.01	$0.50^{+0.02}_{-0.02}$	$1.59^{+1.81}_{-0.54}$	$2.08^{+1.78}_{-0.53}$	
J211507.42-074134.5	6898489884295412352	DA	10622 ± 51	8.42 ± 0.01	0.84 ± 0.01	$0.99^{+0.02}_{-0.02}$	$0.28^{+0.05}_{-0.04}$	$1.28^{+0.05}_{-0.05}$	$0.83^{+0.47}_{-0.25}$
J211507.39-074151.5	6898489884295407488	DA	8131 ± 36	8.19 ± 0.01	0.70 ± 0.01	$1.27^{+0.03}_{-0.02}$	$0.83^{+0.46}_{-0.24}$	$2.10^{+0.47}_{-0.24}$	
J222236.56-082806.0	2616210918121365760	DA	11389 ± 146	8.10 ± 0.01	0.65 ± 0.01	$0.47^{+0.02}_{-0.02}$	$1.66^{+1.87}_{-0.55}$	$2.12^{+1.84}_{-0.55}$	$1.24^{+3.57}_{-1.62}$
J222236.30-082807.9	2616210922414728960	DA	15704 ± 165	8.04 ± 0.01	0.63 ± 0.01	$0.18^{+0.01}_{-0.01}$	$2.55^{+3.36}_{-1.14}$	$2.74^{+3.35}_{-1.15}$	
J222301.62+220131.3	1874954641491354624	DA	19185 ± 245	8.40 ± 0.01	0.84 ± 0.01	$0.20^{+0.01}_{-0.01}$	$0.29^{+0.05}_{-0.05}$	$0.48^{+0.05}_{-0.05}$	$0.52^{+0.28}_{-0.15}$
J222301.72+220124.9	1874954645786146304	DA	13401 ± 91	8.22 ± 0.01	0.72 ± 0.00	$0.38^{+0.01}_{-0.01}$	$0.62^{+0.28}_{-0.15}$	$1.00^{+0.28}_{-0.15}$	
J231941.34+342614.2	1911420636118031744	DA	16601 ± 351	8.08 ± 0.02	0.65 ± 0.01	$0.16^{+0.01}_{-0.01}$	$1.55^{+1.72}_{-0.52}$	$1.72^{+1.69}_{-0.52}$	$1.24^{+2.98}_{-1.29}$
J231941.44+342609.3	1911420636119326976	DA	13882 ± 217	8.06 ± 0.02	0.64 ± 0.01	$0.27^{+0.01}_{-0.01}$	$2.10^{+2.77}_{-0.76}$	$2.38^{+2.75}_{-0.77}$	

Table A2

Age Comparison: This Work versus Heintz et al. (2022)

Object Name	Gaia Source ID (DR3)	Type	Total Age This Work (Gyr)	Total Age Heintz et al. (2022) (Gyr)
J002925.29+001559.7	2543654008364462848	DC	$2.34^{+0.19}_{-0.18}$	$2.46^{+0.04}_{-0.03}$
J002925.62+001552.7	2543653978300417024	DA	$2.11^{+1.59}_{-0.54}$	$1.55^{+0.56}_{-0.25}$
J081427.92+013325.6	3089916403229120640	DA	$1.89^{+0.49}_{-0.33}$	$1.54^{+0.25}_{-0.20}$
J081427.83+013318.7	3089916398933726592	DA	$3.00^{+5.03}_{-0.95}$	$1.77^{+31.10}_{-0.34}$
J102142.06+394225.4	804040486519166976	DA	$2.69^{+1.04}_{-0.45}$	$2.84^{+0.32}_{-0.25}$
J102141.29+394215.5	804040108562044288	DA	$3.33^{+5.00}_{-1.05}$	$2.15^{+2.12}_{-0.23}$
J105242.54+283252.0	731411283875749760	DA	$3.97^{+0.35}_{-0.30}$	$4.75^{+0.13}_{-0.11}$
J105242.57+283255.3	731411283874346240	DQ	$8.16^{+4.34}_{-3.54}$	$2.19^{+0.13}_{-0.17}$
J111322.48+323859.0	757911988004305280	DA	$3.03^{+0.13}_{-0.13}$	$3.13^{+0.06}_{-0.07}$
J111319.38+323818.0	757911884925087104	DA	$3.85^{+3.03}_{-0.85}$	$2.68^{+0.45}_{-0.22}$
J115749.13+313931.0	4026615235380699392	DAH	$2.17^{+0.27}_{-0.25}$	$2.17^{+0.12}_{-0.11}$
J115749.39+313931.0	4026615235380699520	DA	$4.18^{+4.54}_{-1.26}$	$2.60^{+1.17}_{-0.29}$
J115937.82+134408.7	3920275276810355200	DA	$1.51^{+0.07}_{-0.07}$	$1.39^{+0.05}_{-0.07}$
J115937.81+134413.9	3920275276810355072	DA	$1.68^{+0.21}_{-0.10}$	$1.52^{+0.04}_{-0.04}$
J123647.95+682501.6	1682366418152856448	DA	$3.10^{+0.66}_{-0.39}$	$2.76^{+0.14}_{-0.15}$
J123647.42+682502.9	1682554091043762560	DQ	$6.56^{+4.68}_{-3.10}$	$1.32^{+0.03}_{-0.06}$
J134739.13+251228.9	1444442547261998464	DA	$3.50^{+2.46}_{-0.56}$	$3.65^{+9.51}_{-0.96}$
J134737.58+251233.1	1444442512902260864	DA	$2.70^{+2.63}_{-0.63}$	$2.14^{+4.52}_{-0.41}$
J135834.36+263345.2	1450779342012324224	DA	$3.38^{+0.36}_{-0.34}$	$3.61^{+0.28}_{-0.23}$
J135834.66+263343.1	1450779346306149760	DA	$2.02^{+2.64}_{-0.72}$	$1.29^{+1.85}_{-0.45}$
J185722.65+781332.1	2293210651405001216	DA	$3.48^{+4.00}_{-1.05}$	$2.15^{+1.90}_{-0.29}$
J185722.00+781332.2	2293210651402924160	DA	$2.41^{+1.79}_{-0.39}$	$1.98^{+0.19}_{-0.11}$
J213102.82+083203.8	1741031891851063424	DA	$2.88^{+0.23}_{-0.19}$	$2.96^{+0.10}_{-0.10}$
J213103.09+083202.6	1741031896140411648	DA	$3.48^{+3.51}_{-1.24}$	$1.73^{+0.48}_{-0.23}$
J225932.73+140444.2	2815944352131513472	DAH	$1.32^{+0.08}_{-0.07}$	$1.26^{+0.04}_{-0.03}$
J225932.21+140439.2	2815944352131513088	DA	$0.36^{+0.06}_{-0.05}$	$0.30^{+0.02}_{-0.02}$
J231939.16-035857.8	2634002940402436480	DAH	$5.60^{+3.26}_{-1.03}$	$4.63^{+1.99}_{-0.49}$
J231938.65-035833.1	2634003146560869248	DC	$9.60^{+3.57}_{-3.67}$	$2.12^{+0.06}_{-0.08}$
J003051.80+181046.0	2794800060629297152	DA	$0.82^{+0.24}_{-0.09}$	$0.67^{+0.05}_{-0.04}$
J003051.75+181053.7	2794800056333855232	DA	$1.15^{+0.56}_{-0.28}$	$0.80^{+0.10}_{-0.06}$
J080333.78-090705.8	3039398650000089472	DA	$2.73^{+3.10}_{-0.91}$	$1.27^{+0.34}_{-0.17}$
J080333.92-090658.4	3039398650000089600	DC	$2.88^{+2.29}_{-0.61}$	$1.95^{+0.06}_{-0.07}$
J082730.72-021618.5	3072961074934467200	DA	$0.24^{+0.03}_{-0.03}$	$0.17^{+0.02}_{-0.01}$
J082730.58-021620.1	3072961070640767488	DA	$0.41^{+0.07}_{-0.06}$	$0.33^{+0.03}_{-0.04}$
J085917.36+425031.6	1008929564913828224	DA	$2.10^{+1.42}_{-0.54}$	$1.37^{+0.52}_{-0.13}$
J085917.23+425027.4	1008929569208837376	DA	$2.48^{+3.15}_{-0.81}$	$1.18^{+0.60}_{-0.17}$
J092513.18+160145.4	630770819920096768	DA	$0.57^{+0.03}_{-0.03}$	$0.34^{+0.01}_{-0.01}$
J092513.48+160144.1	630770819920096640	DA	$0.36^{+0.05}_{-0.04}$	$0.31^{+0.02}_{-0.03}$
J100244.88+360629.6	795886439568266368	DA	$1.43^{+0.55}_{-0.20}$	$1.17^{+0.07}_{-0.05}$
J100245.86+360653.3	795886439568268032	DA	$3.04^{+4.09}_{-1.07}$	$1.55^{+1.44}_{-0.23}$
J111020.98+451801.7	782193985044906752	DA	$1.33^{+0.69}_{-0.47}$	$0.68^{+0.20}_{-0.08}$
J111016.68+451736.3	782194019404645632	DA	$2.38^{+2.64}_{-0.73}$	$1.21^{+0.36}_{-0.20}$
J122717.81+563821.7	1574653689250595072	DA	$2.55^{+2.40}_{-0.60}$	$2.63^{+10.31}_{-0.79}$
J122717.42+563825.6	1574653689250360576	DA	$1.82^{+2.20}_{-0.61}$	$1.24^{+2.26}_{-0.40}$
J131332.14+203039.6	3940068410255312768	DA	$0.91^{+0.06}_{-0.05}$	$0.83^{+0.02}_{-0.02}$

Table A2
(Continued)

Object Name	Gaia Source ID (DR3)	Type	Total Age This Work (Gyr)	Total Age Heintz et al. (2022) (Gyr)
J131332.56+203039.4	3940068414551140608	DA	$1.32^{+0.46}_{-0.30}$	$0.84^{+0.04}_{-0.04}$
J170355.91+330438.4	1337576648471644800	DA	$1.44^{+0.27}_{-0.13}$	$1.31^{+0.05}_{-0.04}$
J170356.77+330435.7	1337576648471644288	DA	$2.08^{+1.78}_{-0.53}$	$1.22^{+0.27}_{-0.12}$
J211507.42-074134.5	6898489884295412352	DA	$1.28^{+0.05}_{-0.05}$	$1.20^{+0.02}_{-0.02}$
J211507.39-074151.5	6898489884295407488	DA	$2.10^{+0.46}_{-0.24}$	$1.82^{+0.06}_{-0.04}$
J222236.56-082806.0	2616210918121365760	DA	$2.12^{+1.83}_{-0.55}$	$1.03^{+0.08}_{-0.06}$
J222236.30-082807.9	2616210922414728960	DA	$2.76^{+3.33}_{-1.17}$	$1.29^{+0.31}_{-0.27}$
J222301.62+220131.3	1874954641491354624	DA	$0.48^{+0.05}_{-0.05}$	$0.45^{+0.01}_{-0.01}$
J222301.72+220124.9	1874954645786146304	DA	$1.00^{+0.28}_{-0.14}$	$0.78^{+0.02}_{-0.02}$
J231941.34+342614.2	1911420636118031744	DA	$1.72^{+1.70}_{-0.52}$	$1.05^{+0.36}_{-0.22}$
J231941.44+342609.3	1911420636119326976	DA	$2.39^{+2.76}_{-0.78}$	$1.54^{+1.13}_{-0.36}$

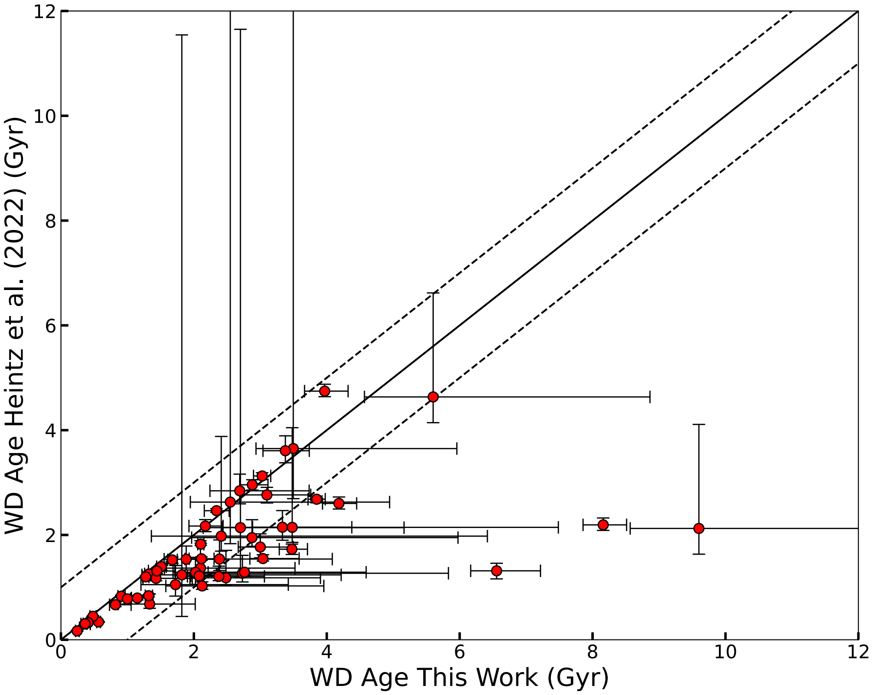

Figure A1. Total age comparison between this work and Heintz et al. (2022). The largest differences are seen for J105242.57+283255.3 (DQ), J123647.42+682502.9 (DQ), and J231938.65−035833.1 (DC).

Table A3

Subgiant−White Dwarf Binaries with Gentile Fusillo et al. (2021) Parameters

SG Gaia Source ID (DR3)	WD Gaia Source ID (DR3)	SG Gmag (mag)	WD Gmag (mag)	WD T_{eff} (K)	WD Mass ($M_\odot$)
4300369510174214784	4300369510169386112	8.81	19.66	12912 ± 3151	0.88 ± 0.25
2336787015926880000	2336787423948155008	9.74	19.82	10624 ± 1785	1.05 ± 0.22
2347362256201579904	2347362359280261248	9.31	20.59	5393 ± 714	0.74 ± 0.37
4392051256453106816	4392051256451595520	7.93	19.56	9787 ± 1344	0.93 ± 0.22
6133033601555979648	6133033635916500608	5.61	16.18	6799 ± 72	0.76 ± 0.02
2119845400308940160	2119845361652709376	10.22	19.74	9260 ± 1733	0.88 ± 0.29
3830984079252585600	3830990156631488128	7.93	17.09	10431 ± 232	0.88 ± 0.03
3831183812411727616	3831183705037343744	7.72	18.95	8640 ± 1671	0.87 ± 0.29
5383783218258538112	5383783355697619840	11.03	20.15	10578 ± 2019	0.93 ± 0.3
6598562289267096448	6598562289266484480	8.35	20.43	5148 ± 1119	0.82 ± 0.77
2376772955294340992	2376773024012888832	9.81	20.07	10685 ± 2125	1.19 ± 0.19
6716346883984454400	6716346888277566080	10.14	19.75	11886 ± 3455	0.99 ± 0.29
2285623681871320320	2285623677575389824	10.01	20.37	11346 ± 3863	0.95 ± 0.43
4331764106188333184	4331764106187008000	7.45	19.10	9549 ± 1056	0.92 ± 0.17
1360094169868916224	1360094169867063168	9.22	20.54	5160 ± 977	0.72 ± 0.45
2033936051408038144	2033937086539674752	9.92	20.67	7640 ± 1658	1.1 ± 0.29
6212459675847218816	6212459710206960256	8.66	18.31	10230 ± 568	0.83 ± 0.08
2879667068210826752	2879667033851088896	6.40	17.77	6386 ± 119	0.78 ± 0.04
2090626428561466112	2090626428557671424	10.04	19.93	9118 ± 2034	0.86 ± 0.35
2027675161648624768	2027675092907621760	9.34	19.36	8146 ± 948	0.83 ± 0.2
554338410851013248	554338410851400576	10.91	20.52	10763 ± 3263	1.07 ± 0.47
1103672557732637568	1103673313648946176	8.58	18.97	11932 ± 2263	1.08 ± 0.14
1959369925890722688	1959369925890724352	8.88	19.51	9603 ± 964	0.89 ± 0.17
5768161698670783104	5768161728731408512	8.54	18.82	7483 ± 443	0.89 ± 0.09
2777818000458834816	2777818069178793216	9.05	20.11	5760 ± 674	0.76 ± 0.28
522824414744038656	522824517819155840	8.72	18.48	9697 ± 938	0.85 ± 0.14
4908881095134079744	4908884011415732608	9.13	19.33	9796 ± 940	0.83 ± 0.16
2245852830169628288	2245852834465778048	9.43	19.47	11546 ± 3274	0.93 ± 0.29
5531471338089757824	5531471342386268544	9.73	20.04	9566 ± 2096	0.93 ± 0.33
2550020872178776448	2550020872178380416	8.57	19.59	5755 ± 682	0.74 ± 0.26
6860685689529683072	6860685689529693312	7.41	18.73	9142 ± 1267	0.91 ± 0.2
5007222548993285376	5007222342833916032	9.81	19.81	7372 ± 1112	0.8 ± 0.27
5046646500480419328	5046645023010375040	9.95	19.87	8318 ± 1438	0.86 ± 0.28
2153552647245580544	2153552814748001792	9.29	19.82	10247 ± 2200	1.11 ± 0.2
816035200601793664	816035402464238592	9.45	20.33	7496 ± 1330	0.82 ± 0.35
4454777398385627904	4454777398385626368	9.30	19.03	7912 ± 465	0.82 ± 0.11
1485875894904733312	1485852491629542144	8.79	18.90	6641 ± 250	0.74 ± 0.07
3158711368312044800	3158709955270315776	8.94	19.46	9766 ± 1785	1.02 ± 0.24
4940783321935202944	4940783321935203200	9.14	18.83	18169 ± 4619	1.22 ± 0.09
508792687856955136	508792687857693952	9.92	20.34	9360 ± 1488	1.0 ± 0.25
1583002147896863360	1583002113536258304	8.73	20.48	5362 ± 687	0.84 ± 0.32
1591057651117375104	1591057681181908736	9.06	18.73	8010 ± 284	0.87 ± 0.06
5643049095188961024	5643047613413300736	10.59	19.84	11115 ± 1586	0.86 ± 0.23
4742627996346980352	4742627996345892096	8.93	20.28	6065 ± 1232	1.05 ± 0.3
4972150528953711872	4972150533247866240	9.95	20.46	7144 ± 2109	1.07 ± 0.88
77232655968062080	77232862125996160	9.41	19.72	7457 ± 1380	0.97 ± 0.27
4573348766683678208	4573348693667903616	8.69	19.88	6400 ± 519	0.9 ± 0.15
2231263620836219520	2231263616542725120	9.80	19.68	9333 ± 1109	0.91 ± 0.19
1044069612939035904	1044069612939334272	8.72	19.42	5881 ± 289	0.75 ± 0.11
4358360983226863616	4358361356891222784	8.85	20.10	4961 ± 574	0.74 ± 0.29
5606450613704556288	5606450579335008128	8.98	19.38	6935 ± 400	0.76 ± 0.12
2185083715854536320	2185083715855943552	11.16	20.42	9306 ± 2503	0.91 ± 0.45
4564212134294495360	4564212061278453248	8.35	18.86	7703 ± 453	0.88 ± 0.1
531850305690610688	531850374406289664	8.56	19.01	6337 ± 473	0.75 ± 0.14
4476374207640229888	4476374108856134656	11.24	19.71	12003 ± 2607	0.86 ± 0.29
5371977010298123264	5371977010295931392	9.96	19.81	8742 ± 1447	0.79 ± 0.29
1656598027422451456	1656598027420856448	9.19	20.01	6605 ± 964	0.84 ± 0.26
4280947595034458496	4280947973002608128	8.98	20.10	7635 ± 1587	0.79 ± 0.4
2939426178022960128	2939426173722815872	9.57	19.79	7256 ± 893	0.85 ± 0.23
4213545852929485056	4213545848628209152	9.91	19.56	8351 ± 819	0.79 ± 0.19
3177760888297880192	3177761094456310656	7.05	17.37	8403 ± 502	0.92 ± 0.08
2455561896956826112	2455561896955810432	8.79	19.56	6122 ± 721	0.74 ± 0.27
1430714491754808832	1430714496049436928	9.24	18.84	14791 ± 5960	0.99 ± 0.23
5198065190247097728	5198065228903571584	10.12	20.00	6931 ± 892	0.75 ± 0.27
5520033535248373120	5520033569597820544	8.69	20.03	7093 ± 1076	0.94 ± 0.24

ORCID iDs

Manuel Barrientos https://orcid.org/0000-0002-6153-9304
Mukremin Kilic https://orcid.org/0000-0001-6098-2235
Pierre Bergeron https://orcid.org/0000-0003-2368-345X
Simon Blouin https://orcid.org/0000-0002-9632-1436
Warren R. Brown https://orcid.org/0000-0002-4462-2341
Jeff J. Andrews https://orcid.org/0000-0001-5261-3923

References

Abrikosov, A. A. 1960, JETP, 39, 1798
Alzate, J. A., Bruzual, G., & Díaz-González, D. J. 2021, MNRAS, 501, 302
Andrews, J. J., Agüeros, M., Brown, W. R., et al. 2016, ApJ, 828, 38
Andrews, J. J., Agüeros, M. A., Gianninas, A., et al. 2015, ApJ, 815, 63
Bailer-Jones, C. A. L., Rybizki, J., Fouesneau, M., Demleitner, M., & Andrae, R. 2021, AJ, 161, 147
Barlow, R. 2003, arXiv:physics/0306138
Barrientos, M., & Chanamé, J. 2021, ApJ, 923, 181
Bauer, E. B. 2023, ApJ, 950, 115
Bédard, A., Bergeron, P., Brassard, P., & Fontaine, G. 2020, ApJ, 901, 93
Bédard, A., Blouin, S., & Cheng, S. 2024, Natur, 627, 286
Bergeron, P., Dufour, P., Fontaine, G., et al. 2019, ApJ, 876, 67
Blouin, S., & Daligault, J. 2021, ApJ, 919, 87
Blouin, S., Daligault, J., & Saumon, D. 2021, ApJL, 911, L5
Blouin, S., Dufour, P., Thibeault, C., & Allard, N. F. 2019, ApJ, 878, 63
Blouin, S., Shaffer, N. R., Saumon, D., & Starrett, C. E. 2020, ApJ, 899, 46
Camisassa, M. E., Althaus, L. G., Córsico, A. H., et al. 2019, A&A, 625, A87
Camisassa, M. E., Althaus, L. G., Torres, S., et al. 2021, A&A, 649, L7
Capitanio, L., Lallement, R., Vergely, J. L., Elyajouri, M., & Monreal-Ibero, A. 2017, A&A, 606, A65
Cassisi, S., Potekhin, A. Y., Pietrinferni, A., Catelan, M., & Salaris, M. 2007, ApJ, 661, 1094
Catalán, S., Isern, J., García-Berro, E., et al. 2008, A&A, 477, 213
Chambers, K. C., Magnier, E. A., Metcalfe, N., et al. 2016, arXiv:1612.05560
Cheng, S., Cummings, J. D., & Ménard, B. 2019, ApJ, 886, 100
Chiba, M., & Beers, T. C. 2000, AJ, 119, 2843
Choi, J., Dotter, A., Conroy, C., et al. 2016, ApJ, 823, 102
Coutu, S., Dufour, P., Bergeron, P., et al. 2019, ApJ, 885, 74
Cummings, J. D., Kalirai, J. S., Tremblay, P. E., Ramirez-Ruiz, E., & Choi, J. 2018, ApJ, 866, 21
Cunningham, T., Tremblay, P.-E., & O'Brien, M, M. W. 2024, MNRAS, 527, 3602
Dufour, P., Blouin, S., Coutu, S., et al. 2017, in ASP Conf. Ser. 509, 20th European White Dwarf Workshop, ed. P. E. Tremblay, B. Gaensicke, & T. Marsh (San Francisco, CA: ASP), 3
El-Badry, K., Rix, H.-W., & Heintz, T. M. 2021, MNRAS, 506, 2269
Fantin, N. J., Côté, P., McConnachie, A. W., et al. 2019, ApJ, 887, 148
Fleury, L., Caiazzo, I., & Heyl, J. 2022, MNRAS, 511, 5984
Fontaine, G., Brassard, P., & Bergeron, P. 2001, PASP, 113, 409
Gaia Collaboration, Brown, A. G. A., Vallenari, A., et al. 2018, A&A, 616, A1
García-Berro, E., Torres, S., Althaus, L. G., et al. 2010, Natur, 465, 194
Gentile Fusillo, N. P., Tremblay, P. E., Cukanovaite, E., et al. 2021, MNRAS, 508, 3877
Giammichele, N., Charpinet, S., Fontaine, G., et al. 2018, Natur, 554, 73
Heintz, T. M., Hermes, J. J., El-Badry, K., et al. 2022, ApJ, 934, 148
Hollands, M. A., Littlefair, S. P., & Parsons, S. G. 2024, MNRAS, 527, 9061
Kilic, M., Bergeron, P., Blouin, S., et al. 2024, arXiv:2403.08878
Kilic, M., Bergeron, P., Kosakowski, A., et al. 2020, ApJ, 898, 84
Kiman, R., Xu, S., Faherty, J. K., et al. 2022, AJ, 164, 62
Kirzhnits, D. A. 1960, JETP, 11, 365
Lallement, R., Vergely, J. L., Valette, B., et al. 2014, A&A, 561, A91
Laursen, P., Sommer-Larsen, J., Milvang-Jensen, B., Fynbo, J. P. U., & Razoumov, A. O. 2019, A&A, 627, A84
Mestel, L. 1952, MNRAS, 112, 583
Mor, R., Robin, A. C., Figueras, F., Roca-Fàbrega, S., & Luri, X. 2019, A&A, 624, L1
Moss, A., Bergeron, P., Kilic, M., et al. 2024, MNRAS, 527, 10111
Rebassa-Mansergas, A., Maldonado, J., Raddi, R., et al. 2021, MNRAS, 505, 3165
Rebassa-Mansergas, A., Maldonado, J., Raddi, R., et al. 2023, MNRAS, 526, 4787
Salpeter, E. E. 1961, ApJ, 134, 669
Saumon, D., Blouin, S., & Tremblay, P.-E. 2022, PhR, 988, 1
Schmidt, G. D., Weymann, R. J., & Foltz, C. B. 1989, PASP, 101, 713
Tremblay, P.-E., Fontaine, G., Gentile Fusillo, N. P., et al. 2019, Natur, 565, 202
Tremblay, P. E., Kalirai, J. S., Soderblom, D. R., Cignoni, M., & Cummings, J. 2014, ApJ, 791, 92
van Horn, H. M. 1968, ApJ, 151, 227
Venner, A., Blouin, S., Bédard, A., & Vanderburg, A. 2023, MNRAS, 523, 4624
Williams, K. A., Canton, P. A., Bellini, A., et al. 2018, ApJ, 867, 62
Winget, D. E., Kepler, S. O., Campos, F., et al. 2009, ApJL, 693, L6